J|A|C|S
ARTICLES
Published on Web 01/26/2007

Spectroscopic and Electronic Structure Study of the Enzyme−Substrate Complex of Intradiol Dioxygenases: Substrate Activation by a High-Spin Ferric Non-heme Iron Site

Monita Y. M. Pau,[†] Mindy I. Davis,[†] Allen M. Orville,[‡,§] John D. Lipscomb,*[,‡] and Edward I. Solomon*[,†]

Contribution from the Department of Chemistry, Stanford University, Stanford, California 94305-5080, and Department of Biochemistry, Molecular Biology and Biophysics and Center for Metals in Biocatalysis, University of Minnesota, Minneapolis, Minnesota 55455

Received August 4, 2006; E-mail: edward.solomon@stanford.edu

Abstract: Various mechanisms have been proposed for the initial O_2 attack in intradiol dioxygenases based on different electronic descriptions of the enzyme−substrate (ES) complex. We have examined the geometric and electronic structure of the high-spin ferric ES complex of protocatechuate 3,4-dioxygenase (3,4-PCD) with UV/visible absorption, circular dichroism (CD), magnetic CD (MCD), and variable-temperature variable-field (VTVH) MCD spectroscopies. The experimental data were coupled with DFT and INDO/S-CI calculations, and an experimentally calibrated bonding description was obtained. The broad absorption spectrum for the ES complex in the 6000−31000 cm^{-1} region was resolved into at least five individual transitions, assigned as ligand-to-metal charge transfer (LMCT) from the protocatechuate (PCA) substrate and Tyr408. From our DFT calculations, all five LMCT transitions originate from the PCA and Tyr π_{op} orbitals to the ferric dπ orbitals. The strong π covalent donor interactions dominate the bonding in the ES complex. Using hypothetical Ga^{3+}-catecholate/semiquinone complexes as references, 3,4-PCD-PCA was found to be best described as a highly covalent Fe^{3+}-catecholate complex. The covalency is distributed unevenly among the four PCA valence orbitals, with the strongest interaction between the π_{op-sym} and Fe d_{xz} orbitals. This strong π interaction, as reflected in the lowest energy PCA-to-Fe^{3+} LMCT transition, is responsible for substrate activation for the O_2 reaction of intradiol dioxygenases. This involves a multi-electron-transfer (one β and two α) mechanism, with Fe^{3+} acting as a buffer for the spin-forbidden two-electron redox process between PCA and O_2 in the formation of the peroxy-bridged ESO_2 intermediate. The Fe ligand field overcomes the spin-forbidden nature of the triplet O_2 reaction, which potentially results in an intermediate spin state ($S = {}^3/_2$) on the Fe^{3+} center which is stabilized by a change in coordination along the reaction coordinate.

1. Introduction

Like heme-containing enzymes, mononuclear non-heme iron-containing enzymes perform a wide range of important biological functions,[1−5] but their reaction mechanisms are generally less well understood. This is true in part because the non-heme enzymes lack the convenient spectroscopic probe provided by the intense porphyrin $\pi \rightarrow \pi^*$ absorption features of heme enzymes. In recent years, significant progress has been made in understanding the geometric and electronic structures of the active sites of mononuclear non-heme iron enzymes and their contributions to the molecular mechanisms.[4−6] A good example of this is found in the non-heme oxygenase family, which uses the active-site metal to activate O_2 for reaction with organic substrates. Although the uncatalyzed reactions of triplet O_2 with singlet organic substrates are thermodynamically favorable, they are very slow because they are spin forbidden. Activation of O_2 via reduction is also slow due to the low one-electron reduction potential of O_2. Most non-heme oxygenases catalyze O_2 activation using a high-spin Fe^{2+} site through a redox process that also involves the substrate or an additional cofactor to provide the required number of electrons. These include extradiol dioxygenases, pterin-dependent hydroxylases, α-ketoglutarate-dependent enzymes, and Rieske dioxygenases. In contrast, a small group of the non-heme iron-containing enzymes employ a high-spin Fe^{3+} site to activate substrate for direct attack by O_2. The primary examples of this type of enzyme are the lipoxygenases and intradiol dioxygenases, which is the enzyme class of interest in this paper.

[†] Stanford University.
[‡] University of Minnesota.
[§] Current address: Biology Department, Brookhaven National Laboratory, Upton, NY 11973.

(1) Feig, A. L.; Lippard, S. J. *Chem. Rev.* **1994**, *94*, 759−805.
(2) Hegg, E. L.; Que, L., Jr. *Eur. J. Biochem.* **1997**, *250*, 625−629.
(3) Lipscomb, J. D.; Orville, A. M. In *Degradation of Environmental Pollutants by Microorganisms and Their Metalloenzymes*; Sigel, H., Sigel, A., Eds.; Marcel Dekker, Inc.: New York, 1992; pp 243−298.
(4) Que, L., Jr.; Ho, R. Y. N. *Chem. Rev.* **1996**, *96*, 2607−2624.
(5) Solomon, E. I.; Brunold, T. C.; Davis, M. I.; Kemsley, J. N.; Lee, S. K.; Lehnert, N.; Neese, F.; Skulan, A. J.; Yang, Y. -S.; Zhou, J. *Chem. Rev.* **2000**, *100*, 235−349.
(6) Neidig, M. L.; Solomon, E. I. *Chem. Commun.* **2005**, 5843−5863.

10.1021/ja065671x CCC: $37.00

Scheme 1. Intradiol Cleavage of PCA by 3,4-PCD

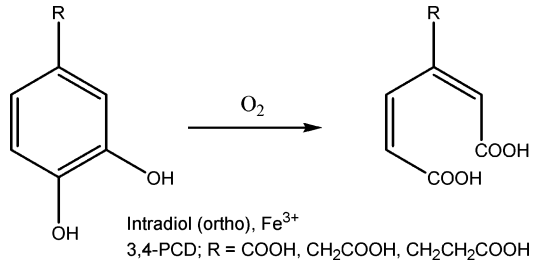

Intradiol dioxygenases belong to a large class of enzymes called catecholic dioxygenases.[3] These widely distributed enzymes catalyze the cleavage of molecular oxygen, accompanied by insertion of both oxygen atoms into the aromatic ring of the substrate, resulting in ring cleavage. The bacterial catecholic dioxygenases are important in the aerobic biodegradation of aromatic compounds, including the recalcitrant pollutant polychlorinated biphenyls (PCBs).[7−10] The catecholic dioxygenases fall into two structurally and mechanistically distinct classes, "extradiol" and "intradiol". While extradiol dioxygenases utilize an Fe^{2+} (and occasionally Mn^{2+})[11−13] center to cleave the ring on either the distal or the proximal side of the vicinal hydroxyl groups of the substrate, intradiol dioxygenases employ an Fe^{3+} center to catalyze the cleavage of the aromatic ring between the hydroxylated carbon atoms.[3−5,14,15]

Protocatechuate 3,4-dioxygenase (3,4-PCD, EC 1.13.11.3) is one of the most extensively studied intradiol dioxygenases. It catalyzes the ring cleavage of protocatechuate (PCA, 3,4-dihydroxybenzoate) to form β-carboxy-*cis*,*cis*-muconate, with the incorporation of both oxygen atoms from molecular oxygen[16] (Scheme 1). X-ray crystal structures are available for the resting form and various mutants, as well as in a number of ligand complexes with substrate, substrate analogues, inhibitors, and oxygen analogues of 3,4-PCD isolated from *Pseudomonas aeruginosa* (now reclassified as *putida*) and *Acinetobacter calcoaceticus* ADP1.[17−22] The enzyme has also been isolated and spectroscopically characterized from *Brevibacterium fuscum*,[23] which has the most highly resolved spectroscopic features of any intradiol dioxygenase. Crystallographic and X-ray absorption (XAS)[24,25] data show that the resting state of 3,4-PCD contains a high-spin ferric center in a distorted trigonal-bipyramidal geometry, with Tyr447 and His462 as the axial ligands and Tyr408, His460, and a hydroxide ligand defining the equatorial plane (residue numbering from the *P. putida* enzyme). Upon anaerobic substrate binding, the active site shifts to a square-pyramidal geometry and the axial Tyr447 and equatorial OH^- are displaced by the substrate, which binds bidentate in its doubly deprotonated form.[26] The open coordination position is trans to His460, and the substrate binds asymmetric to the Fe^{3+} center, with the longer bond trans to the equatorial Tyr408.[20]

The catalytic reaction mechanism of 3,4-PCD shows a sequential order, with PCA binding before dioxygen. On the basis of a series of experimental data on the substrate- and inhibitor-bound 3,4-PCD complexes as well as the intermediates observed during the substrate and inhibitor binding step,[19,20,27,28] it has been proposed that PCA initially binds monodentate with the deprotonated 4-OH of PCA. Through ligand rearrangement, PCA^{O4} shifts to the axial position trans to His462, displaces Tyr447, which assists in the deprotonation of the 3-OH, and allows PCA^{O3} to bind to the Fe^{3+} site in the equatorial plane trans to Tyr408 (Scheme 2).

Based on different electronic descriptions of the enzyme−substrate (ES) complex, various mechanisms have been proposed for the substrate activation step of the initial O_2 attack in the enzymatic reaction: (1) Fe^{2+}-semiquinone with O_2 attacking the iron site, (2) Fe^{2+}-semiquinone with O_2 attacking the substrate through radical coupling, and (3) Fe^{3+}-catecholate with strong ketonized character promoted by lengthening the Fe−PCA^O bond from the trans influence from Tyr408 and the O_2 interacting directly with the substrate through electrophilic attack[29−35] (Scheme 2). No matter which mechanism is adopted, the net result of the O_2 attack is thought to be the formation of a peroxy adduct between the iron site and one of the hydroxylated carbons, accompanied by a spin-forbidden two-electron transfer from the electron pair of the substrate to the triplet O_2 molecule. Since the differences among the mechanistic proposals lie in the electronic structure description of the enzyme−substrate, it is important to determine the nature of this ES complex, particularly its degree of radical character. This would allow elucidation of the mechanism of substrate activation and

(7) Dagley, S. In *The Bacteria*; Sokatch, J. R., Ornston, L. N., Eds.; Academic Press, Inc.: Orlando, FL, 1986; Vol. 10, Chapter 10, pp 527−555.
(8) Levin, M. A.; Gealt, M. A. In *Biotreatment of Industrial and Hazardous Waste*; Levin, M. A., Gealt, M. A., Eds.; McGraw-Hill, Inc.: New York, 1993; pp 5−7.
(9) Glick, B. R.; Pasternak, J. J. *Molecular Biotechnology: Principles and Applications of Recombinant DNA*, 2nd ed.; American Society for Microbiology: Washington DC, 1998.
(10) Hrywna, Y.; Tsoi, T. V.; Maltseva, O. V.; Quensen, J. F., III; Tiedje, J. M. *Appl. Environ. Microbiol.* **1999**, *65*, 2163−2169.
(11) Boldt, Y. R.; Sadowsky, M. J.; Ellis, L. B. M.; Que, L., Jr.; Wackett, L. P. *J. Bacteriol.* **1995**, *177*, 1225−1232.
(12) Que, L., Jr.; Widom, J.; Crawford, R. L. *J. Biol. Chem.* **1981**, *256*, 10941−10944.
(13) Whiting, A. K.; Boldt, Y. R.; Hendrich, M. P.; Wackett, L. P.; Que, L., Jr. *Biochemistry* **1996**, *35*, 160−170.
(14) Bugg, T. D. H.; Winfield, C. J. *Nat. Prod. Rep.* **1998**, 513−530.
(15) Bugg, T. D. H.; Lin, G. *Chem. Commun.* **2001**, 941−952.
(16) Fujisawa, H.; Hayaishi, O. *J. Biol. Chem.* **1968**, *243*, 2673−2681.
(17) Elgren, T. E.; Orville, A. M.; Kelly, K. A.; Lipscomb, J. D.; Ohlendorf, D. H.; Que, L., Jr. *Biochemistry* **1997**, *36*, 11504−11513.
(18) Frazee, R. W.; Orville, A. M.; Dolbeare, K. B.; Yu, H.; Ohlendorf, D. H.; Lipscomb, J. D. *Biochemistry* **1998**, *37*, 2131−2144.
(19) Orville, A. M.; Elango, N.; Lipscomb, J. D.; Ohlendorf, D. H. *Biochemistry* **1997**, *36*, 10039−10051.
(20) Orville, A. M.; Lipscomb, J. D.; Ohlendorf, D. H. *Biochemistry* **1997**, *36*, 10052−10066.
(21) Vetting, M. W.; D'Argenio, D. A.; Ornston, L. N.; Ohlendorf, D. H. *Biochemistry* **2000**, *39*, 7943−7955.
(22) Valley, M. P.; Brown, C. K.; Burk, D. L.; Vetting, M. W.; Ohlendorf, D. H.; Lipscomb, J. D. *Biochemistry* **2005**, *44*, 11024−11039.
(23) Whittaker, J. W.; Lipscomb, J. D.; Kent, T. A.; Münck, E. *J. Biol. Chem.* **1984**, *259*, 4466−4475.
(24) Davis, M. I.; Wasinger, E. C.; Westre, T. E.; Zaleski, J. M.; Orville, A. M.; Lipscomb, J. D.; Hedman, B.; Hodgson, K. O.; Solomon, E. I. *Inorg. Chem.* **1999**, *38*, 3676−3683.
(25) True, A. E.; Orville, A. M.; Pearce, L. L.; Lipscomb, J. D.; Que, L., Jr. *Biochemistry* **1990**, *29*, 10847−10854.
(26) Horsman, G. P.; Jirasek, A.; Vaillancourt, F. H.; Barbosa, C. J.; Jarzecki, A. A.; Xu, C. L.; Mekmouche, Y.; Spiro, T. G.; Lipscomb, J. D.; Blades, M. W.; Turner, R. F. B.; Eltis, L. D. *J. Am. Chem. Soc.* **2005**, *127*, 16882−16891.
(27) Bull, C.; Ballou, D. P.; Otsuka, S. *J. Biol. Chem.* **1981**, *256*, 12681−12686.
(28) Whittaker, J. W.; Lipscomb, J. D. *J. Biol. Chem.* **1984**, *259*, 4476−4486.
(29) Que, L., Jr.; Lipscomb, J. D.; Munck, E.; Wood, J. M. *Biochim. Biophys. Acta* **1977**, *485*, 60−74.
(30) Cox, D. D.; Que, L., Jr. *J. Am. Chem. Soc.* **1988**, *110*, 8085−8092.
(31) Jang, H. G.; Cox, D. D.; Que, L., Jr. *J. Am. Chem. Soc.* **1991**, *113*, 9200−9204.
(32) Lipscomb, J. D.; Orville, A. M.; Frazee, R. W.; Dolbeare, K. B.; Elango, N.; Ohlendorf, D. H. In *Spectroscopic Methods in Bioinorganic Chemistry*; Solomon, E. I., Hodgson, K. O., Eds.; American Chemical Society: Washington, DC, 1998; pp 387−402.
(33) Funabiki, T.; Yamazaki, T. *J. Mol. Catal. A: Chem.* **1999**, *150*, 37−47.
(34) Funabiki, T.; Konishi, T.; Kobayashi, S.; Mizoguchi, A.; Takano, M.; Yoshida, S. *Chem. Lett.* **1987**, 719−722.
(35) Hitomi, Y.; Yoshida, M.; Higuchi, M.; Minami, H.; Tanaka, T.; Funabiki, T. *J. Inorg. Biochem.* **2005**, *99*, 755−763.

Scheme 2. Proposed Mechanism for 3,4-PCD

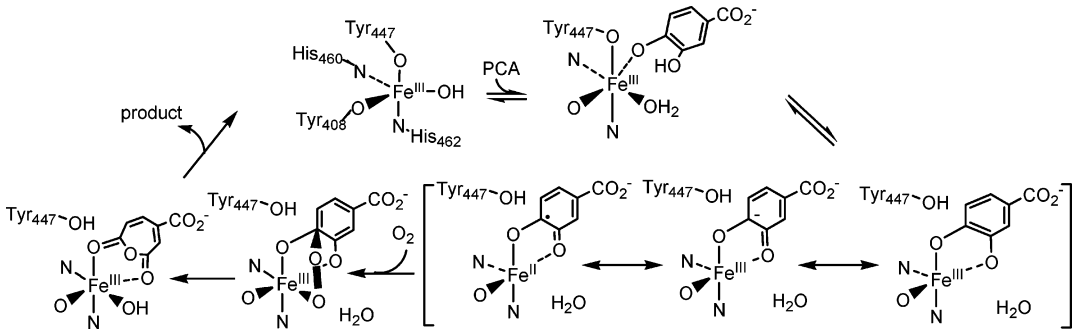

define how the intradiol dioxygenases overcome the spin forbidden nature of the O_2 ring-opening reaction.

Some insight into the electronic structure of the ES complex has been derived from previous spectroscopic studies. All EPR and Mössbauer studies have shown that 3,4-PCD remains high-spin ferric upon substrate binding.[23,25,36] Substrate-free 3,4-PCD has an intensive absorption feature at 460 nm, characteristic of a tyrosine-to-Fe^{3+} charge-transfer (CT) transition.[16] This has been studied in detail in ref 37. Upon anaerobic substrate binding, a new broad, low-energy feature appears at ~600 nm, and Raman excitation into this new band indicates that it arises from catecholate-to-Fe^{3+} CT.[17,38] This low-energy catecholate-to-Fe^{3+} CT suggests that covalency in the ES complex can be key to the substrate activation mechanism. The presence of two non-innocent ligands (Tyr408 and substrate) in the ES complex results in a broad absorption envelope with a series of overlapping ligand-to-metal charge-transfer (LMCT) transitions. In this study, we employ UV/visible absorption (UV/vis Abs), circular dichroism (CD), and low-temperature magnetic CD (MCD) along with variable-temperature variable-field MCD (VTVH MCD) to resolve individual bands in the broad absorption spectrum. The experimental data were coupled with density functional theory (DFT) and INDO/S-CI calculations to determine the electronic structure of the ES complex of 3,4-PCD and to correlate it with the geometric structure. The frontier molecular orbitals involved in substrate activation in intradiol dioxygenases were identified and provide insight into the two-electron spin-forbidden reaction between O_2 and the catecholic substrate.

2. Experimental Section

2.1. Sample Preparation. All commercial reagents were of the highest grade available and used without further purification unless otherwise specified. Protocatechuate 3,4-dioxygenase from *Brevibacterium fuscum* was purified as previously reported, stored at −80 °C, and thawed immediately prior to use.[23,39] The Abs and CD spectra and other selected comparisons of 3,4-PCD isolated from *P. putida* and *B. fuscum* were identical in both the oxidized and the reduced forms.[24,40] Therefore, it is reasonable to compare the spectroscopic results on *B. fuscum* 3,4-PCD (which exhibits the most well-resolved features) to the crystal structures of *P. putida* 3,4-PCD. The 100 mM 3-(*N*-morpholino)propanesulfonic acid buffer (MOPS, Sigma) was prepared with deionized water and adjusted to pH 7.0 with NaOH (Sigma). Protocatechuic acid (PCA, 3,4-dihydroxybenzoic acid, Aldrich) and homoprotocatechuic acid (HPCA, 3,4-dihydroxyphenylacetic acid, Aldrich) were purified by sublimation, with the samples being heated under vacuum in a flask equipped with a coldfinger cooled by dry ice. Once purified, these were stored under N_2 in the dark.

All samples were prepared under an inert atmosphere in an Mbraun Labmaster 100 glovebox maintained at less than 1 ppm O_2. The protein was rigorously degassed at 4 °C in a Teflon-stoppered glass vial by evacuating and back-filling 20 times with Ar that had been passed over a copper catalyst (BASF) to remove residual O_2. Buffers were degassed under vacuum by freeze/pump/thaw/heat procedures. The catecholic substrates were weighed in small glass vials, transferred to the glovebox, and dissolved in MOPS buffer. Enzyme−substrate samples were prepared by adding a small aliquot of substrate solution anaerobically to the protein to give 15-fold excess substrate and incubated for 15 min. For the MCD experiments, 50% (v/v) glycerol, degassed under vacuum by freeze/pump/thaw/heat procedures, was added as a glassing agent. CD and Abs spectra were taken with and without glycerol present to ensure that the protein was unaffected by the glassing agent. MOPS buffer was prepared in D_2O (99.9 atom % D; Cambridge Isotope Laboratories) and adjusted to a pD of 6.6. NaOD (Sigma) and glycerol-d_3 (98 atom % D; Cambridge Isotope Laboratories) were used to eliminate the hydroxide overtones that dominate the IR absorption spectrum above 1600 nm.

2.2. Spectroscopic Studies. UV/vis Abs spectra were recorded on an HP8452A diode array spectrometer at room temperature and on a Cary 17 spectrometer equipped with a Janis Research Super Vari-temp helium cryogenic Dewar mounted in the light path at 5 K. CD and MCD data were collected on CD spectropolarimeters with modified sample compartments to accommodate magnetocryostats. The near-IR data were collected on a Jasco J-200D instrument with a liquid N_2-cooled InSb detector coupled to an Oxford Instruments SM4000-7T magnetocryostat. The UV/vis data were collected either on a Jasco J-500C instrument coupled to an Oxford Instruments SM4-7T magnetocryostat or a Jasco J-810 instrument coupled to an Oxford Instruments SM4000-8T magnetocryostat. Both UV/vis spectropolarimeters are equipped with extended S-20/S-1 photomultiplier tubes (Hamamatsu).

Room-temperature Abs and CD samples were prepared in a 0.5 cm path length quartz anaerobic cuvette and kept at 4 °C at all times with a circulating cooling bath attached to the sample holder. Buffer and cell baselines were subtracted from the raw protein Abs and CD spectra. Low-temperature (1.6−50.2 K) Abs and MCD spectra were obtained in a copper MCD sample cell with two Infrasil quartz disks sandwiching a 3 mm thick neoprene O-ring spacer into which the sample was injected. The samples were frozen in liquid N_2 immediately after preparation. The depolarization of the frozen sample was checked by measuring the CD spectrum of a nickel (+)-tartrate solution placed before and after the sample and was less than 5%.[41]

(36) Que, L., Jr.; Lipscomb, J. D.; Zimmerman, R.; Münck, E.; Orme-Johnson, N. R.; Orme-Johnson, W. H. *Biochim. Biophys. Acta* **1976**, *452*, 320−334.
(37) Davis, M. I.; Orville, A. M.; Neese, F.; Zaleski, J. M.; Lipscomb, J. D.; Solomon, E. I. *J. Am. Chem. Soc.* **2002**, *124*, 602−614.
(38) Fujisawa, H.; Hiromi, K.; Uyeda, M.; Okuno, S.; Nozaki, M.; Hayaishi, O. *J. Biol. Chem.* **1972**, *247*, 4422−4428.
(39) Whittaker, J. W.; Orville, A. M.; Lipscomb, J. D. *Methods Enzymol.* **1990**, *188*, 82−88.
(40) Orville, A. M.; Lipscomb, J. D. *Biochemistry* **1997**, *36*, 14044−14055.

The MCD spectra were corrected for the natural CD and zero-field baseline effects caused by glass strain by subtracting the 0 T scans from each of the field scans at a given temperature. The Abs, CD, and MCD spectra were iteratively fit to Gaussian band shapes by using a modified Levenberg−Marquardt constrained least-squares fitting routine. For VTVH MCD spectroscopy, a calibrated Cernox resistor (Lakeshore Cryotronics, calibrated 1.5−300 K) inserted in the sample cell was used to accurately measure the temperature of the sample. VTVH data were normalized to the maximum observed intensity and were analyzed using the theory and associated fitting program developed in ref 42.

2.3. Electronic Structure Calculations. A. Active-Site Geometry. The active-site geometric structures of 3,4-PCD-PCA and 3,4-PCD-HPCA were obtained from the averaged crystallographic coordinates of *P. putida* 3,4-PCD complexed with PCA (PDB code 3PCA) and HPCA (PDB code 3PCN), respectively.[17,20] Hydrogen atoms were placed at standard bond lengths and angles. DFT calculations were performed on a model of 3,4-PCD-PCA with two Me-imidazoles to model His460 and His462, 4-Me-phenolate to model Tyr408, and a bidentate PCA in the fully deprotonated state. Second-sphere residues which interact with the substrate, Arg457, Tyr324, and Trp449, were also modeled in as methyl-guanidium ion, 4-Me-phenolate, and 3-Me-indole, respectively. Semiempirical calculations were performed on the 3,4-PCD-HPCA complex with a simpler model: two imidazoles to model the two histidines, phenolate to model the tyrosine residue, and a dianionic HPCA.

B. DFT Calculations. Spin-unrestricted DFT calculations were performed using Gaussian 03[43] to geometry optimize the 102-atom active model described above. The double-ξ LanL2DZ basis set was used in all geometry optimizations with two commonly used functionals: Becke's 1988 exchange functional with the correlation function of Perdew (BP86)[44,45] as well as Becke's three-parameter hybrid functional with the correlation function of Lee, Yang, and Parr (B3LYP).[46−48] The 102-atom model was partially optimized with the coordinates of the β-carbon of the backbone and all heavy atoms in the second-sphere residues held constant to simulate the protein pocket. Frequencies and thermodynamic parameters were calculated, and all frequencies were found to be real except where constraints were imposed. The charges were calculated using natural population analysis (NPA).[49] Solvation effects were included using the polarized continuum model (PCM)[50] with a dielectric constant $\epsilon = 4.0$ to model the protein environment. In all calculations, convergence was reached when the relative change in the density matrix between subsequent iterations was less than 1×10^{-8}.

To correlate calculations to experimental excited-state data, time-dependent (TD) DFT calculations[51−53] were carried out for the geometry-optimized model in Gaussian 03. The two second-sphere residues which interact with the tail of the substrate were removed to minimize computational time. In order to cover the entire energy range of interest, 150 excitations were calculated. Excitation energies for the same model were also calculated with the Slater transition method[54,55] in the Amsterdam density functional (ADF 2004) program developed by Baerends et al.[56−58] The local density approximation (LDA) of Vosko and co-workers[59] was used along with gradient corrections of Becke for the exchange and of Perdew for the correlation (BP86). The calculations were spin-polarized, and the basis set used for all atoms was an uncontracted triple-ξ basis set (TZP) with a single polarization function without any frozen core approximation. This program does not provide an option to generate hybrid functionals. Hence, in order to experimentally evaluate the calculations, spin-unrestricted single-point calculations for the model optimized in Gaussian 03 were performed using the ADF package, and the nuclear charge on Fe (Z_{Fe}) was varied from 26 to 25.8. The ground-state wave functions were used as initial guesses to obtain excited-state wave functions, where half an electron was transferred from an occupied to an unoccupied orbital. Excitation energies were calculated as differences between the two partially occupied orbitals. Calculations were accepted as converged when the relative change in the density matrix between subsequent iterations was less than 10^{-5}. Solvent effects were included using the conductor-like screening model (COSMO),[60−62] and the protein environment was modeled using a dielectric constant $\epsilon = 4.0$. Spin densities obtained from the experimentally calibrated calculation in ADF were then matched in Gaussian 03 with various amounts of Hartree−Fock (HF) exchange mixing into the BP86 functional. Molecular orbitals obtained from both Gaussian 03 and ADF calculations were analyzed using the AOMix program,[63,64] and the graphical output of the computational results was generated with Molden (Gaussian) and gOpenMol (ADF).

3. Results and Analysis

3.1. Absorption, CD, and Low-Temperature MCD Spectroscopy. Abs, CD, and low-temperature MCD spectra for 3,4-PCD-HPCA and 3,4-PCD-PCA are shown in Figures 1 and 2. CD spectra taken with and without the glassing agent glycerol present were found to be unchanged. The Gaussian resolution obtained by simultaneously fitting the Abs, CD, and MCD data of 3,4-PCD-HPCA indicates the presence of at least five transitions in the 6000−31000 cm^{-1} region (Figure 1). All the observed transitions are assigned as LMCT, as all d→d transitions are spin-forbidden in this high-spin d^5 system. The energies, Abs ϵ, and MCD $\Delta\epsilon$ are given in Table 1. VTVH data were collected for bands 1−5. It is important to note the presence of both positive and negative bands in the MCD spectrum, as this is an indication of pseudo-A-term behavior. Similar to 3,4-PCD-HPCA, the Gaussian resolution of Abs, CD, and MCD data of 3,4-PCD-PCA indicates the presence of at least five transitions in the 6000−31000 cm^{-1} region (Figure 2). The energies, Abs ϵ, and MCD $\Delta\epsilon$ are also shown in Table 1. VTVH data were collected for bands 1, 3, 4, and 5. No VTVH data were collected for negative band 2 due to its low intensity, which can be attributed to a partial cancellation effect from two

(41) Browett, W. R.; Fucaloro, A. F.; Morgan, T. V.; Stephens, P. J. *J. Am. Chem. Soc.* **1983**, *105*, 1868−1872.
(42) Neese, F.; Solomon, E. I. *Inorg. Chem.* **1999**, *38*, 1847−1865.
(43) Frisch, M. J.; et al. *Gaussian 03*, Revision C.02; Gaussian Inc.: Wallingford, CT, 2004.
(44) Becke, A. D. *Phys. Rev. A: Gen. Phys.* **1988**, *38*, 3098−3100.
(45) Perdew, J. P. *Phys. Rev. B: Condens. Matter Mater. Phys.* **1986**, *33*, 8822−8824.
(46) Lee, C.; Yang, W.; Parr, R. G. *Phys. Rev. B: Condens. Matter Mater. Phys.* **1988**, *37*, 785−789.
(47) Miehlich, B.; Savin, A.; Stoll, H.; Preuss, H. *Chem. Phys. Lett.* **1989**, *157*, 200−206.
(48) Becke, A. D. *J. Chem. Phys.* **1993**, *98*, 5648−5652.
(49) Reed, A. E.; Curtiss, L. A.; Weinhold, F. *Chem. Rev.* **1988**, *88*, 899−926.
(50) Cramer, C. J.; Truhlar, D. G. *Chem. Rev.* **1999**, *99*, 2161−2200.
(51) Casida, M. E. In *Recent Advances in Density Functional Theory*; Chong, D. P., Ed.; World Scientific: Singapore, 1995; Vol. 1, p 155.
(52) Gross, E. U. K. In *Density Functional Theory*; Nalewajski, R. F., Ed.; Springer: Heidelberg, 1996.
(53) Stratmann, R. E.; Scuseria, G. E.; Frish, M. J. *J. Chem. Phys.* **1998**, *109*, 8218−8224.
(54) Slater, J. C. *The Self-Consistent Field for Molecules and Solids: Quantum Theory of Molecules and Solids*; McGraw Hill: New York, 1974.
(55) Slater, J. C. *The Calculation of Molecular Orbitals*; John Wiley & Sons: New York, 1979.
(56) Baerends, E. J.; Ellis, D. E.; Ros, P. *Chem. Phys.* **1973**, *2*, 41−51.
(57) Versluis, L.; Ziegler, T. *J. Chem. Phys.* **1988**, *88*, 322−328.
(58) Te Velde, G.; Baerends, E. J. *J. Comput. Phys.* **1992**, *99*, 84−98.
(59) Vosko, S. H.; Wilk, L.; Nusair, M. *Can. J. Phys.* **1980**, *58*, 1200−1211.
(60) Klamt, A.; Schuurmann, G. *J. Chem. Soc., Perkin Trans. 2* **1993**, 799−805.
(61) Klamt, A. *J. Chem. Phys.* **1995**, *99*, 2224−2235.
(62) Klamt, A.; Jonas, V. *J. Chem. Phys.* **1996**, *105*, 9972−9981.
(63) Gorelsky, S.I., *AOMix: Program for Molecular Orbital Analysis*; York University: Toronto, Canada, 1997 (http://www.sg-chem.net/).
(64) Gorelsky, S. I.; Lever, A. B. P. *J. Organomet. Chem.* **2001**, *635*, 187−196.

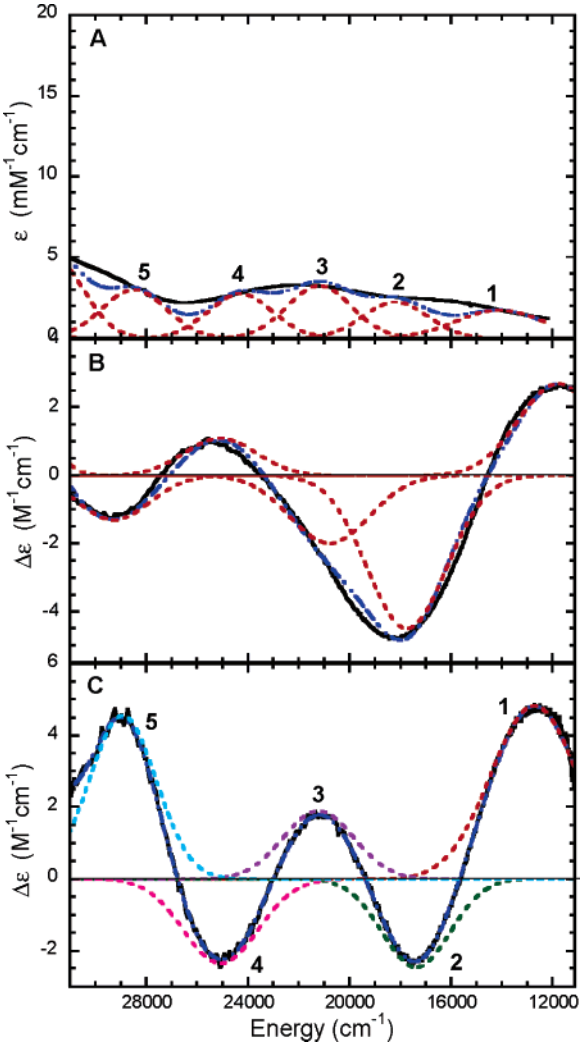

Figure 1. Gaussian resolution (- - -) of spectra (—) of 3,4-PCD-HPCA. (A) Abs at 4 °C, (B) CD at 4 °C, and (C) MCD at 5 K and 1 T.

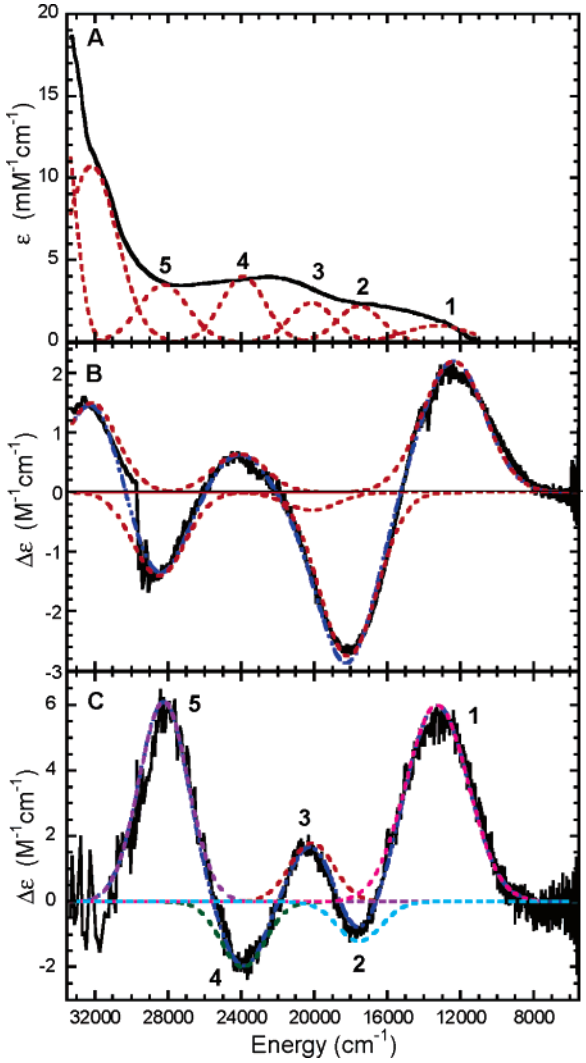

Figure 2. Gaussian resolution (- - -) of spectra (—) of 3,4-PCD-PCA. (A) Abs at 4 °C, (B) CD at 4 °C, and (C) MCD at 5 K and 1 T.

adjacent overlapping intense positive bands. Again, MCD signals of alternating signs are observed, indicating pseudo-A-term behavior among the LMCT transitions. While there are slight shifts in band energies and signal intensities, the spectroscopic data for 3,4-PCD-HPCA and 3,4-PCD-PCA look extremely similar. This indicates that the presence of an extra carbon in the carboxylate tail of the substrate induces only a minimal effect on the Fe center.

3.2. VTVH MCD Spectroscopy and Orientation of the D-Tensor. MCD data were collected at various temperatures and fields for four of the LMCT transitions of 3,4-PCD-PCA and five of the LMCT transitions of 3,4-PCD-HPCA. The data were collected at or near the maxima of the Gaussian-resolved bands so as to minimize contributions from overlapping bands. The data were normalized and plotted as a function of $\beta H/2k_BT$ (Figures 3 and 4), where β is the Bohr magneton and k_B is the Boltzmann constant. The nesting (i.e., spread) observed for the different isotherms is expected for a Kramers system with zero-field splitting (ZFS), and the features are identified by their temperature dependence as MCD C-terms. Two types of saturation magnetization behavior are observed in the four sets of VTVH MCD data collected on 3,4-PCD-PCA. Bands 1 and 5 have very similar saturation magnetization behavior: the MCD signals saturate quickly and the isotherms have very limited nesting. The saturation magnetization behaviors of bands 3 and 4 are also very similar: the MCD signals do not saturate at 7 T, and the isotherms are more nested than those of bands 1 and 5. For 3,4-PCD-HPCA, three types of saturation magnetization behavior are observed in the five sets of VTVH MCD data collected. Bands 1 and 5 have very similar saturation magnetization behavior: MCD signals saturate quickly, and the isotherms have very limited nesting. For band 2, each isotherm

Table 1. Gaussian Resolution and Experimental Parameters for the Observed Transitions of 3,4-PCD-HPCA and 3,4-PCD-PCA

band	Abs energy (cm^{-1})	ϵ (mM^{-1} cm^{-1})	MCD energy (cm^{-1})	$\Delta\epsilon$ (M^{-1} cm^{-1})
		3,4-PCD-HPCA		
1	14 100	1.8	12 700	4.83
2	18 200	2.3	17 400	−2.46
3	21 200	3.3	21 200	1.89
4	24 300	2.8	25 100	−2.34
5	28 500	3.0	28 900	4.56
		3,4-PCD-PCA		
1	13 300	1.0	13 400	5.97
2	17 550	2.2	17 600	−1.20
3	20 150	2.4	20 200	1.78
4	23 900	4.0	24 000	−1.94
5	28 250	3.5	28 300	6.10

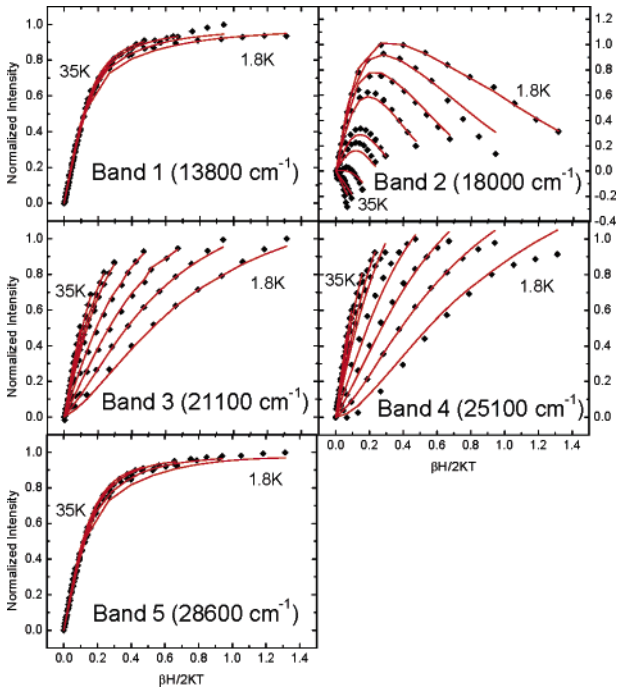

Figure 3. VTVH MCD data for 3,4-PCD-HPCA. The fits are shown in red.

passes through a maximum with variation in $\beta H/2k_BT$, and significant nesting behavior is observed. For bands 3 and 4, the MCD signals do not saturate at 7 T, and the isotherms are more nested than those in bands 1 and 5. It is important to note that the two types of saturation magnetization behavior noted in 3,4-PCD-PCA, namely that of bands 1 and 5, and that of bands 3 and 4, are very similar to those of the corresponding bands in 3,4-PCD-HPCA.

VTVH MCD data can be fitted by using a theoretical approach based upon the spin Hamiltonian.[42] The model relates the nonlinear MCD behavior to both transition polarization and the spin expectation values of the different ZFS sublevels for $S \geq {}^1/_2$ in low-symmetry molecular environments as given below:

$$\frac{\Delta\epsilon}{E} = \frac{\gamma}{4\pi S}\int_0^{\pi}\int_0^{2\pi}\sum_i N_i(l_z\langle S_z\rangle_i M_{xy}^{\mathrm{eff}} + l_y\langle S_y\rangle_i M_{xz}^{\mathrm{eff}} + l_x\langle S_x\rangle_i M_{yz}^{\mathrm{eff}})\sin\theta\,\mathrm{d}\theta\,\mathrm{d}\phi \quad (1)$$

where x, y, and z refer to the principal axes of the ZFS tensor; θ and ϕ are the polar angles between the incident light and the molecular z-axis; l_x, l_y, and l_z are the direction cosines for the magnetic field relative to the molecular coordinate system; M_{ij}^{eff} are the products of the polarizations of the electronic transitions; and γ is a collection of constants. Equation 1 is also dependent on N_i, the Boltzmann population, and $\langle S_p\rangle_i$, the spin expectation value in the p direction for the spin sublevels i of the ground state. Two perpendicular transition moments, i and j, are required for MCD intensity. In a low-symmetry protein site, a transition is unidirectional, so $M_{ij}^{\mathrm{eff}} \neq 0$ is accomplished by spin−orbit mixing with another excited state that has a perpendicularly polarized transition moment. By obtaining the spin-Hamiltonian parameters D, E/D, and g_p from EPR data (which give the energy and $\langle S_p\rangle$ of the different sublevels), the effective transition moment products M_{ij}^{eff} can be determined

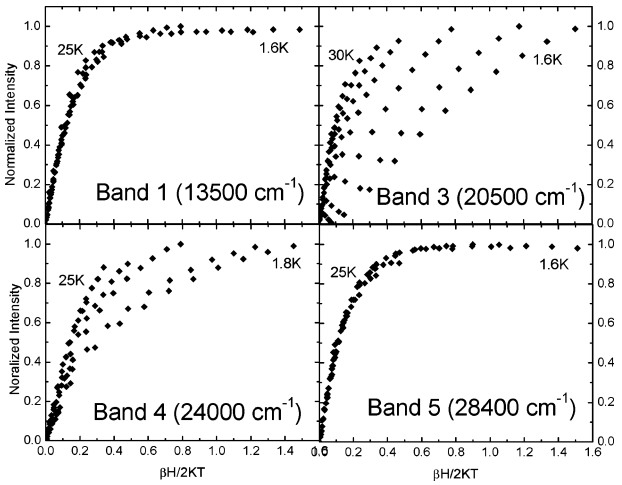

Figure 4. VTVH MCD data for 3,4-PCD-PCA.

from eq 1. Using these effective transition moment products, the percent polarization along the ZFS tensor axes for each transition can then be determined with eq 2 (with cyclic permutations of indices for the remaining two directions).

$$\%x = 100 \times \left[\frac{(M_{xy}^{\mathrm{eff}}\,M_{xz}^{\mathrm{eff}})^2}{(M_{xy}^{\mathrm{eff}}\,M_{xz}^{\mathrm{eff}})^2 + (M_{xy}^{\mathrm{eff}}\,M_{yz}^{\mathrm{eff}})^2 + (M_{yz}^{\mathrm{eff}}\,M_{xz}^{\mathrm{eff}})^2}\right] \quad (2)$$

Previous EPR studies showed that 3,4-PCD-PCA is composed of a mixture of species with E/D values ranging from the axial limit (0) to the rhombic limit (0.33).[23,36] The heterogeneity in ground states complicates spectral analysis, as the amount of each species with a specific E/D would be required to fit the VTVH MCD data. EPR studies were also performed on 3,4-PCD-HPCA, and the data showed only one dominant species (90%) with $E/D = 0.33$ and $|D| = 1.8$ cm^{-1}.[65] Due to the clean ground-state electronic configuration, VTVH MCD analysis was feasible. As mentioned above, spectral data and saturation magnetization behavior for all CT bands in 3,4-PCD-PCA are qualitatively very similar to those in 3,4-PCD-HPCA. Thus, the spectral assignments are expected to be the same for these two complexes.

To analyze the VTVH MCD data for 3,4-PCD-HPCA, the signs of D and E are important for determining polarizations, as shown in our previous study in 3,4-PCD.[37] In the rhombic limit for $S = {}^5/_2$, the effective g-values for the first and third Kramers doublets, $g(1)_{x,y,z}$ and $g(3)_{x,y,z}$, are pairwise identical but with their order interchanged with opposite signs of D. For high-spin ferric complexes, the true g-values are isotropic, the **g**-matrix and **D**-tensor are collinear, and hence, a change in the order of the effective g-values (i.e., the sign of D) leads to an interchange of two of the polarization directions.

INDO/S-CI calculations were performed to determine the signs of the D and E values for 3,4-PCD-HPCA. The **D**-tensor was mapped onto the coordinates of the 3,4-PCD-HPCA active site by calculating the second-order spin−orbit coupling of the $^6A_1$ ground state over the entire excited-state manifold of $^4T_1$ and $^6T_1$ states, as described in ref 66. By diagonalizing the **D**-tensor, the principal values D_{xx}, D_{yy}, and D_{zz} are determined, and the spin-Hamiltonian parameters ($D = D_{zz} - {}^1/_2(D_{xx} + D_{yy})$,

(65) Orville, A. M.; Lipscomb, J. D. *J. Biol. Chem* **1989**, *264*, 8791−8801.
(66) Neese, F.; Solomon, E. I. *Inorg. Chem.* **1998**, *37*, 6568−6582.

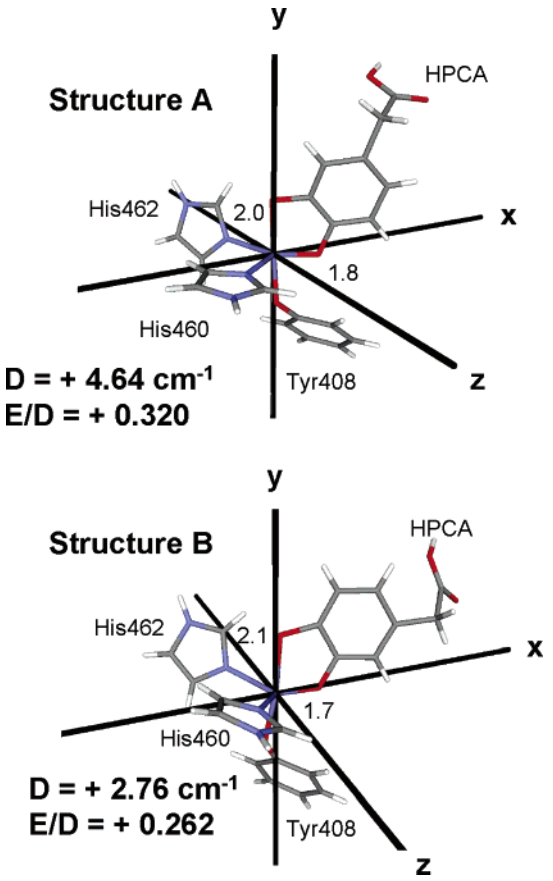

Figure 5. ZFS tensor for 3,4-PCD-HPCA (structures A and B). Asymmetric Fe−O^{HPCA} bond lengths in Å are included.

Table 2. Effective Transition Moments and Percent Polarization from the VTVH MCD Data of 3,4-PCD-HPCA

band	M_{xy}	M_{xz}	M_{yz}	% *x*	% *y*	% *z*
1	0.54	1.06	0.33	66.5	6.6	26.9
2	−4.94	1.75	1.04	71.6	25.3	3.2
3	0.68	−0.18	2.01	0.7	92.8	6.5
4	−2.09	0.25	−1.48	2.9	95.7	1.4
5	0.47	0.97	0.37	56.1	8.3	35.6

$E = {}^1/_2(D_{xx} - D_{yy})$) are calculated. Two structures (A and B) were determined in the 2.4 Å resolution crystallographic studies which differ only in the orientation of the substrate HPCA.[17] INDO/S-CI calculations were performed on both structures, and the orientations of their **D**-tensors were found to be similar, with the *x*-direction oriented along the shorter O^{HPCA}−iron bond, the *y*-direction along the tyrosinate−iron bond, and the *z*-direction oriented closest to one of the histidine−iron bonds (Figure 5). The spin-Hamiltonian parameters showed only minor differences, with *D* and *E* values being positive for both structures ($D = +4.64$ cm^{-1}, $E/D = +0.32$ for structure A and $D = +2.76$ cm^{-1}, $E/D = +0.26$ for structure B).

Using the values for $|D|$, E/D, and *g* determined from EPR and the signs of *D* and *E* determined from INDO/S-CI calculations, the M_{ij}^{eff} values were obtained with eq 1, and the percent *x*, *y*, and *z* polarizations, as defined by the principal directions of the **D**-tensor (Figure 5), of the CT transitions of 3,4-PCD-HPCA were calculated with eq 2. The results are given in Table 2. Consistent with the qualitative analysis, bands 1 and 5 have the same polarization, namely 67% and 56% *x*-polarized, respectively. VTVH fitting reveals that band 2 is also *x*-polarized (72%) and both bands 3 and 4 are *y*-polarized (93% and 96%, respectively). CT transitions are polarized along the associated ligand−metal bond. By mapping the directions of the **D**-tensor obtained from the INDO/S-CI calculations onto the molecular coordinate frame, polarization information obtained from VTVH MCD analysis can be interpreted in terms of a specific ligand−metal bond. With the O^{HPCA}−iron bond oriented along the *x*-direction and the tyrosinate−iron bond along the *y*-direction, bands 1, 2, and 5 are assigned as O^{HPCA}−iron LMCT, and bands 3 and 4 are assigned as tyrosinate−iron LMCT. This assignment is consistent with previous resonance Raman data[17] which showed that band 2 arises from HPCA and band 3 is associated with the tyrosinate ligand. Due to the similarity of the spectroscopic data between 3,4-PCD-PCA and 3,4-PCD-HPCA, the same assignment can be applied to the 3,4-PCD-PCA complex, and hence, bands 1, 2, and 5 are assigned as O^{PCA}−iron LMCT and bands 3 and 4 are tyrosinate−iron LMCT transitions.[67]

Table 3. Experimental and Calculated Geometric Parameters of the 3,4-PCD-PCA Complex

bond length (Å)	crystal structure	BP86	B3LYP
Fe−$O3^{PCA}$	2.49	2.15	2.13
Fe−$O4^{PCA}$	2.04	2.00	2.10
Fe−O^{Tyr408}	1.94	1.90	1.90
Fe−N^{His462}	2.19	2.16	2.17
Fe−N^{His460}	2.21	2.11	2.14
O3−$C3^{PCA}$	1.36	1.40	1.36
O4−$C4^{PCA}$	1.39	1.36	1.33

3.3. Electronic Structure Calculations. DFT calculations were performed on the active site of 3,4-PCD-PCA to gain insight into the electronic structure of this ES complex. The results were correlated to the spectroscopic data, and the origin of the derivative-shaped sign changes throughout the MCD spectrum (pseudo-A-terms) was investigated.

A. Geometry Optimization of the 3,4-PCD-PCA Complex. The crystal structure of 3,4-PCD-PCA was truncated to a 102-atom model, which consists of both first- and second-coordination-sphere residues of the active site. Attempts at geometry-optimizing the ES complex by including only the first-coordination-sphere residues failed to reproduce the unique substrate geometry observed in the crystal structure. The second-sphere residues included interact with the substrate through either hydrogen-bonding or steric interactions, which are very likely to affect the geometry of the substrate. This model was geometry optimized with BP86 and B3LYP using LanL2DZ as the basis set, and the results along with existing crystallographic data[20] are summarized in Table 3. Good agreement with the crystal structure was found with both functionals, except that the Fe−O_3^{PCA} bond lengths were underestimated in both cases. The 2.2 Å resolution crystallographic data showed clear evidence of inequivalent Fe−O^{PCA} bonds with PCA in a non-planar conformation. While both functionals reproduced the folded geometry of PCA, significant inequivalence in the Fe−O^{PCA} bonds was found only in the calculation with BP86 (0.15

(67) Among the seven LMCT transitions observed in the UV/vis Abs spectrum of resting 3,4-PCD, three have been assigned as Tyr408→Fe^{3+} LMCTs.[37] Only two Tyr408→Fe^{3+} LMCTs are observed in the ES complex, and the energies are different from those in the resting enzyme (Figure S1). This can be attributed to changes in (1) the ligand system (Tyr447 and OH^- vs catecholate) and (2) the active-site geometry from trigonal-bipyramidal to square-pyramidal.

Table 4. Compositions of the Spin-Down MOs for the Ground-State Wave Function of the ES Complex[a]

MO no.	energy (eV)	label	% Fe d	% Tyr			% PCA				
				π_{op}	π_{ip}	total	π_{op-sym}	$\pi_{op-asym}$	π_{ip-sym}	$\pi_{ip-asym}$	total
147	−1.66	x^2-y^2	71.4		3.52	7.5				8.1	12.8
146	−2.58	z^2	78.7			1.8	1.1		3.1		5.6
145	−3.06	xy	79.9	3.4	5.2	9.7	4.5		2.5		7.9
144	−3.24	yz	74.5	9.8		11.6	6.0				7.5
143	−3.42	xz	77.0	1.9		1.9	8.1	4.9			14.4
142	−4.22	PCA π_{op-sym}	10.2			1.4	31.5	7.4	2.7		87.1
141	−4.45	PCA π_{op-sym}	6.3	2.4		3.2	34.3	2.8			88.9
139	−4.87	Tyr π_{op}	11.9	70.4		80.6		2.1			5.6
137	−5.25	PCA $\pi_{op-asym}$	1.9			1.2	1.7	47.4		1.8	95.8
134	−6.06	PCA $\pi_{ip-asym}$	1.9		35.1	43.2			19.4	20.3	49.9
132	−6.23	PCA π_{ip-sym}	4.6		1.1	1.6			30.3	25.5	66.7
131	−6.48	Tyr π_{ip}	11.8		36.8	41.8			14.9	10.2	30.3

[a] Geometry optimized with BP86/LanL2DZ in Gaussian and wave function obtained with ADF BP86 with $Z_{Fe} = 25.8$ and $\epsilon = 4.0$ (COSMO).

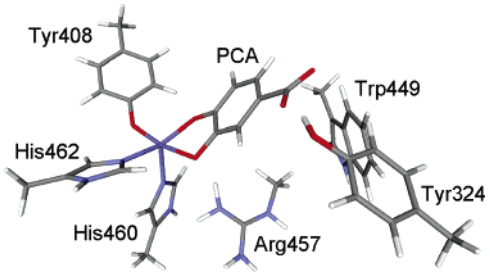

Figure 6. Geometry-optimized model of the 3,4-PCD-PCA active site obtained with Gaussian BP86 and LanL2DZ as basis set.

Å in BP86 vs 0.03 Å in B3LYP).[68] Hence, further investigation into the electronic structure of the ES complex was performed on the geometry-optimized model obtained with the BP86 functional (Figure 6).

B. Electronic Structure of ES Complex. The ground-state orbital energies and one-electron wave functions obtained with the experimentally calibrated DFT protocol (ADF: BP86/TZP with $Z_{Fe} = 25.8$ and $\epsilon = 4.0$, *vide infra*) on the model optimized with BP86 and LanL2DZ in Gaussian are summarized in Table 4.[69] The **D**-tensor principal axes obtained from INDO/S-CI calculations are chosen as the coordinate system for all DFT calculations, with the *x*-direction oriented along the shorter O^{PCA}−iron bond, the *y*-direction along the tyrosinate−iron bond, and the *z*-direction oriented closest to one of the histidine−iron bonds, which is approximately along the axial direction of the square-pyramidal structure.

The energy level diagram and MOs for the optimized structure are shown in Figures 7 and 8, respectively. The five lowest-energy unoccupied MOs in the β spin manifold display predominantly iron 3d character, with the LUMO having substantial mixing with the catecholate ligand. Because of spin polarization, their five occupied counterparts in the α manifold are greatly stabilized in energy by ∼4 eV. This suggests the active site consists of a high-spin ferric center with strong

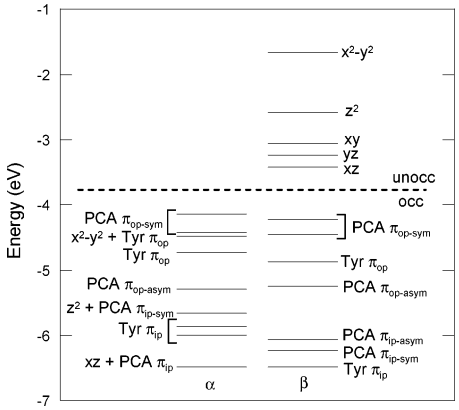

Figure 7. Energy level diagram of the 3,4-PCD-PCA complex. Geometry optimized with BP86/LanL2DZ in Gaussian and wave function obtained with ADF BP86 with $Z_{Fe} = 25.8$ and $\epsilon = 4.0$ (COSMO). Only three of the occupied α Fe d orbitals are shown; the remaining two are at lower energy, below the range shown in this figure.

covalent interactions with the catecholate ligand. The splitting pattern of the d orbitals of 3,4-PCD-PCA is consistent with the square-pyramidal geometry observed in crystal and geometry-optimized structures, with $d_{xz} < d_{yz} < d_{xy} < d_{z^2} < d_{x^2-y^2}$. The presence of the Fe−O^{Tyr} π bond as well as the longer Fe−O^{PCA} bond along the *y*-direction makes the d_{yz} orbital slightly less stable than the d_{xz} orbital.

The high-lying occupied ligand orbitals which dominate the bonding interactions with the iron d orbitals are the valence orbitals from the tyrosinate and catecholate ligands (Figure 9). Free phenolate and catecholate ligands have three filled 2p orbitals on each oxygen atom. While the oxygen 2p orbital directed along the C−O bond is involved in σ bonding to the carbon atom, the remaining two oxygen 2p orbitals have significant contributions in the π_{ip} and π_{op} molecular orbitals, where π_{ip} lies in the plane of the aromatic ring and π_{op} lies perpendicular to the aromatic ring. Depending on the ∠Fe−O−C and the Fe−O−C−C dihedral angle, these two π orbitals can interact with the iron d orbitals through σ or π bonding, as discussed in detail in our previous study on the resting 3,4-PCD site.[37] For the catecholate ligand, the π_{ip} orbitals on the two oxygen atoms can be either in-phase (symmetric, sym) or out-of-phase (antisymmetric, asym) and similarly for the π_{op} orbitals, resulting in four different MOs on the catecholate. For a free catecholate ligand, the energy ordering of these four donor orbitals is $\pi_{op-asym} < \pi_{ip-asym} < \pi_{ip-sym} < \pi_{op-sym}$, and they can participate in either σ or π interactions with the iron d

(68) Both are more symmetric than the 0.45 Å difference observed in the crystal structure. Our optimizations were done with fixed second-sphere residues and in vacuum. Removing the constraints on Arg increases the inequivalence to 0.27 Å (BP86/LanL2DZ). If the Fe−O^{PCA} bond lengths are fixed to 2.04 and 2.49 Å as in the crystal structure while the rest of the molecule is allowed to geometry optimize, the final geometric and electronic structures are essentially the same as those in our more symmetric model, and the energy cost for this asymmetry is only 2.5 kcal/mol.

(69) The wave function and electronic description obtained with BP86/LanL2DZ in Gaussian is qualitatively very similar to that obtained with the spectroscopically calibrated protocol. Hence, we present only the calibrated results here.

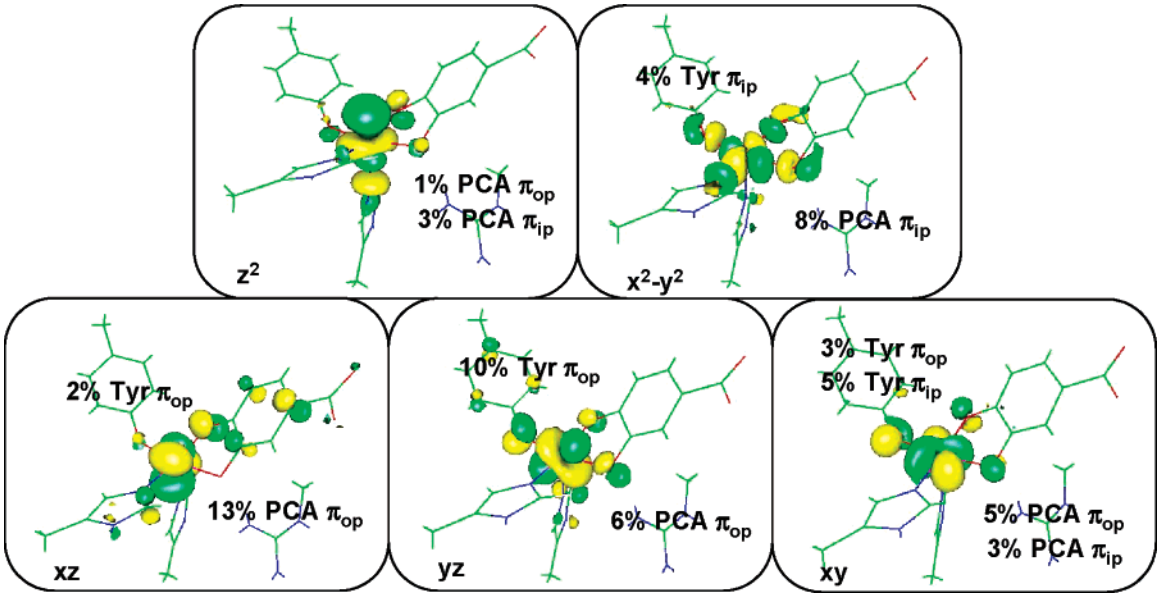

Figure 8. Contours for the five unoccupied β Fe d orbitals of 3,4-PCD-PCA complex. Geometry optimized with BP86/LanL2DZ in Gaussian and wave function obtained with ADF BP86 with $Z_{Fe} = 25.8$ and $\epsilon = 4.0$ (COSMO).

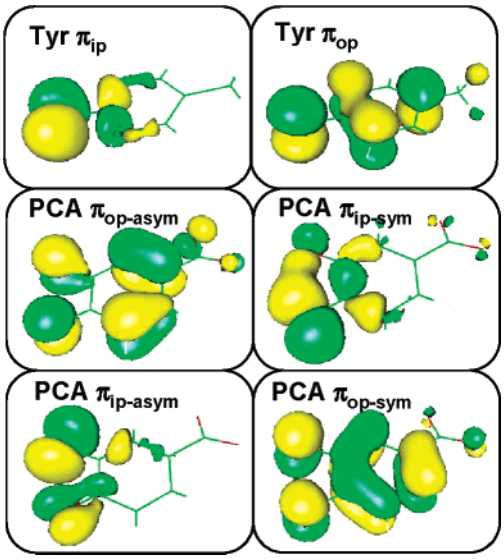

Figure 9. Valence ligand orbitals participating in bonding interactions with Fe.

orbitals, depending on the fold angle between the O−Fe−O plane and the plane of the catechol ligand.

Table 4 summarizes the orbital contributions of the valence metal-based orbitals as well as the relevant high-lying ligand orbitals from the tyrosine and catecholate. Here, we focus on the unoccupied β MOs to evaluate the bonding contributions. They are antibonding with respect to the Fe−L interaction and reflect the uncompensated occupied counterparts which give the major contribution to bonding. Both σ and π bonding interactions with the tyrosinate and catecholate ligands are observed in the ES complex, with d_{xz} and d_{yz} having π antibonding interactions with the tyrosine and catechol π_{op} orbitals, and d_{xy} and $d_{x^2-y^2}$ having σ antibonding interactions with the tyrosine and catechol π_{ip} orbitals. The σ interactions provide the greater stabilization of the π_{ip} orbitals of both catechol and tyrosinate relative to their π_{op} counterparts. The total π_{op} tyrosinate and catecholate characters in both of the d_{xz} and d_{yz} orbitals are much higher than the total π_{ip} characters of the same two ligands in the d_{xy} and $d_{x^2-y^2}$ orbitals; hence, the bonding interaction in the ES complex is dominated by the strong π covalent donor bonds between tyrosine/catechol π_{op} orbitals and the iron d_{xz} and d_{yz} orbitals.[70]

C. Time-Dependent DFT and Slater Transition Calculations: Comparison to Spectroscopic Data. All the experimentally observed transitions are expected to be spin-allowed LMCT in the β manifold. From the energy level diagram, we would expect the lower energy transitions observed experimentally to arise from the π_{op} orbitals of the catecholate and tyrosinate ligands, while transitions from the π_{ip} orbitals will be at much higher energy. TD-DFT calculation with BP86 in Gaussian on the Fe active site with Arg included as a second-sphere residue showed that the lower energy transitions are indeed all due to the π_{op} orbitals of these two ligands, with the lowest CT from the π_{op-sym} catecholate donor, the next from the π_{op} tyrosinate donor, and the higher energy CT from the $\pi_{op-asym}$ catecholate donor orbital (Figure 10). The energy pattern of these calculated CT transitions is consistent with the experimental spectral assignment, which predicts the two lowest energy LMCTs (bands 1 and 2) to arise from catecholate, followed by two LMCTs (bands 3 and 4) from tyrosinate, and with the last LMCT (band 5) arising from catecholate, which we now assign as the $\pi_{op-asym}$ CT. However, the magnitude of the calculated transition energies is $\sim$7000 cm^{-1} lower than the experimental values (Figure 10A). Slater transition-state calculations performed with ADF on the same truncated model show similar results, with the energy ordering of the calculated CT being consistent with experiment but the predicted magnitude shifted $\sim$7000 cm^{-1} to lower energy (Figure 10B, upper). This suggests that the pure functional BP86 is too covalent to describe the ES complex. The observation that pure functionals are often too covalent in describing the metal−ligand bonds in transition metal complexes has also been made in our previous DFT

(70) Although the Fe 4s orbital can overlap with the π_{ip} orbitals of PCA and Tyr to contribute in the bonding interactions, the energy difference between the 4s and ligand orbitals is large ($\sim$8 eV), and this restricts the amount of mixing ($\sim$2%).

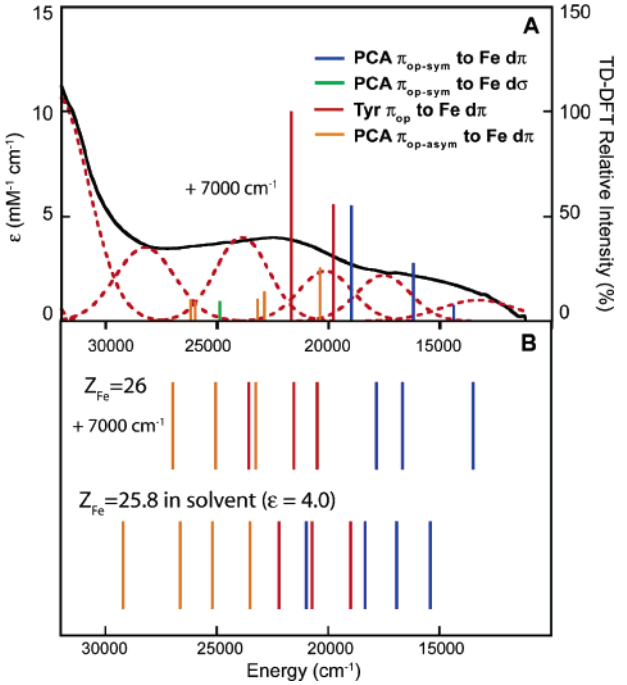

Figure 10. Comparison of the Abs spectrum with calculated transition energies of the 3,4-PCD-PCA complex. (A) Transition energies and intensities predicted by Gaussian TD-DFT. The intensities are indicated by the height of the vertical lines (*y*-axis, right). (B) Transition energies predicted by Slater transitions with ADF (upper, $Z_{Fe} = 26$ in vacuum; lower, $Z_{Fe} = 25.8$ in solvent). Although the calculated energies are 7000 cm^{-1} too low for the TD-DFT and $Z_{Fe} = 26$ Slater transition calculations, the energy ordering of the LMCT agrees with the experimental data.

studies on $CuCl_4^-$ and $S = {}^3/_2$ {FeNO}^{7} complex.[71,72] This leads to too much spin density on the ligand and LMCT transition energies which are too low. To reduce the amount of mixing between the Fe and ligands, Z_{Fe} has decreased from 26 to 25.8. A significant improvement in the calculated values was obtained, with the predicted LMCT now being ~3500 cm^{-1} lower in energy relative to experiment. By taking into account the effects of solvent ($\epsilon = 4.0$), the calculated LMCT falls in the experimental region (within 1500 cm^{-1}) (Figure 10B, lower).

To obtain the same experimentally calibrated electronic description of the ES complex in Gaussian, ionic Hartree−Fock (HF) character was mixed into the covalent DFT wave function to destabilize the Fe d-manifold and improve the ground-state description. Since spin density gives a measurement of covalency and thus the bonding description, spin densities obtained from the spectroscopically calibrated calculation in ADF were compared with those obtained in Gaussian with various amounts of HF exchange mixing in the density functional. A bonding description consistent with experiments is obtained when the spin densities obtained from Gaussian match those obtained from ADF with $Z_{Fe} = 25.8$. The results are summarized in Table 5. Significant difference in spin densities is observed between the Gaussian BP86/LanL2DZ and ADF BP86/TZP calculations. By replacing the effective core potential basis set with TZP, an all-electron basis set, a single-point energy calculation with BP86 in Gaussian now shows spin densities comparable to those obtained using the same functional in ADF. Spin densities

Table 5. Spin Densities of Fe, Tyr, and PCA with Gaussian[a] and ADF on a Fixed Geometry Optimized with BP86/LanL2DZ in Gaussian

	Fe	Tyr	PCA
Gaussian			
BP86/LanL2DZ	3.71	0.33	0.86
BP86/TZP	3.83	0.29	0.81
BP86/TZP/solv	3.95	0.34	0.60
BP86 + 10% HFX/TZP	3.90	0.24	0.81
BP86 + 10% HFX/TZP/solv	4.04	0.30	0.55
BP86 + 20% HFX/TZP	3.94	0.18	0.84
ADF			
$Z_{Fe} = 26$/TZP	3.83	0.29	0.80
$Z_{Fe} = 25.8$/TZP	4.05	0.25	0.65
$Z_{Fe} = 25.8$/TZP/solv	4.20	0.27	0.42

[a] Various amounts of HF exchange (HFX) were mixed into the pure density functional BP86 in the Gaussian calculation.

obtained with BP86/TZP and various amount of HF exchange (0−20%) in Gaussian were compared with the experimentally calibrated value obtained from ADF with $Z_{Fe} = 25.8$ both in vacuum and in the presence of solvent. The best agreement was found with 10% HF exchange. Geometry optimization with BP86 + 10% HF exchange with TZP results in a structure comparable to that obtained from BP86 and LanL2DZ (Figure S2); thus, the choice of functional and basis set has a stronger impact on the bonding description than on the geometry of the ES complex. This establishes the BP86 with 10% HF exchange and the TZP basis set as an experimentally calibrated DFT protocol for further studies on the O_2 reaction of the ES complex. However, TZP is too large a basis set to use for geometry optimization along each step of the reaction coordinate on a practical time scale. Hence, a mixed basis set was introduced for the optimization of the ES complex, where the Fe^{3+} center and residues in the first coordination sphere are described by an all-electron double-ξ basis set, 6-31G*, and the residues in the second coordination sphere are described by the all-electron double-ξ basis set, 3-21G*. The resulting optimized structure is comparable to the structure optimized with BP86 and LanL2DZ (Figure S2), except that the asymmetry in Fe−O^{PCA} bond length is less pronounced and the Tyr residue directly coordinated to the Fe^{3+} is rotated by ~45° relative to the crystal structure. Rotation of the Tyr residue is found to cost only 3 kcal/mol, and these structural differences do not have a significant effect on the calculated spin densities. Hence, the experimentally calibrated DFT protocol for further geometry optimization calculations with the ES complex is the hybrid BP86 + 10% HF exchange with a mixed 6-31G*/3-21G* basis set.

The spin densities on the PCA substrate in the experimentally calibrated calculations (0.65 in ADF with $Z_{Fe} = 25.8$ and 0.81 in Gaussian with 10% HF exchange) appear to suggest that the ES complex has significant Fe^{2+}-semiquinone character. However, covalent interactions with a highly paramagnetic center can also contribute to ligand spin density. The PCA π_{op-sym} orbital character is evaluated in section 3.5A by comparing with catecholate and semiquinone bound to non-paramagnetic Ga^{3+} sites.

3.4. Spin−Orbit Coupling Mechanism for MCD Pseudo-A-Term Behavior. MCD intensity is described by A-, B-, and C-terms.[73−76] For paramagnetic systems, the C-term ($= C_0/kT$)

(71) Szilagyi, R. K.; Metz, M.; Solomon, E. I. *J. Phys. Chem. A* **2002**, *106*, 2994−3007.
(72) Schenk, G.; Pau, M. Y. M.; Solomon, E. I. *J. Am. Chem. Soc.* **2004**, *126*, 505−515.
(73) Stephens, P. J. *J. Chem. Phys.* **1970**, *52*, 3489−3516.

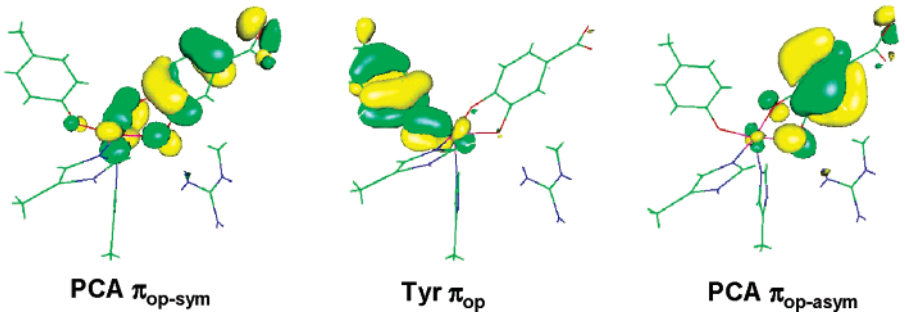

Figure 11. Ligand-based MOs involved in SOC mechanism for MCD pseudo-A-terms. Note the significant metal characters in these orbitals.

dominates the MCD intensity at low temperature. C_0 for a spin-allowed transition from a spatially non-degenerate doublet ground state $|A\rangle$ to an excited state $|J\rangle$ is given by

$$C_0(A\rightarrow J) = -\frac{1}{6}\sum_{uvw} g_w \sum_{K\neq A,J} [\Delta_{KJ}^{-1} L_w^{KJ}(D_u^{KA} D_v^{AJ} - D_v^{KA} D_u^{AJ}) + \Delta_{KA}^{-1} L_w^{KA}(D_u^{AJ} D_v^{JK} - D_v^{AJ} D_u^{JK})] \quad (3)$$

where g_w is the effective g-value of the doublet in the w-direction, L_w^{KA} and L_w^{KJ} are the spin−orbit coupling (SOC) matrix elements in the w-directions, and $D_u^{AJ} = \langle A\ S_{tot}M_S \mid m_v \mid J\ S_{tot}M_S\rangle$ $(= D_u^{JA})$ is the component of the transition dipole moment between $|A\rangle$ and $|J\rangle$ in the u-direction (equivalent definitions for D_u^{KA}, D_v^{AJ}, and D_v^{KA}).[42]

Two mechanisms allow for a non-zero C_0 value in systems with less than C_3 symmetry: (1) SOC between two nearby excited states $|J\rangle$ and $|K\rangle$, to which orthogonal transitions are made from a single ground state $|A\rangle$, and (2) SOC between the ground state $|A\rangle$ and a low-lying excited state $|K\rangle$, from which two orthogonal transitions can be made to a single excited state $|J\rangle$. For the first mechanism, J and K are interchangeable, resulting in the following relationship:

$$C_0(A\rightarrow K) = -C_0(A\rightarrow J) \quad (4)$$

This implies that the two orthogonal transitions $|A\rangle\rightarrow|J\rangle$ and $|A\rangle\rightarrow|K\rangle$ will give rise to oppositely signed C-terms with equal intensities, and this pair of C-terms is the "pseudo-A-term" which obeys the MCD sum rule (i.e., the total MCD intensity summed over all MCD-active excited states is zero).[77] For the second mechanism, at low temperatures, where the low-lying excited state $|K\rangle$ is not populated, only the $|A\rangle\rightarrow|J\rangle$ transition is observed; the $|K\rangle\rightarrow|J\rangle$ transition serves as a virtual orthogonal transition required for MCD activity. This does not obey the MCD sum rule and is not consistent with the spectrum of the 3,4-PCD-PCA complex in Figure 2.

The sign changes for the LMCT in the MCD spectra for both 3,4-PCD-PCA and 3,4-PCD-HPCA reflect pseudo-A-term behavior, which follows the first mechanism for C-term intensity, i.e., SOC between the LMCT excited states. The mechanism of pseudo-A-term behavior between two perpendicularly polarized CT transitions involves SOC along the third mutually orthogonal direction. As shown in our VTVH MCD analysis, all of the observed LMCTs are either x-polarized and originating from PCA or y-polarized and originating from Tyr. For MCD activity, these x- and y-polarized transitions require a SOC matrix element in the z-direction, L_z, and the C_0 parameter in eq 3 can be rewritten as

$$C_0(A\rightarrow J) = -\frac{1}{6}\sum_{K\neq A,J} g_z \Delta_{KJ}^{-1}(D_x^{KA} D_y^{AJ} - D_y^{KA} D_x^{AJ}) L_z^{KJ} \quad (5)$$

Since the SOC is effectively a localized, one-center, one-electron operator, the center involved in SOC using L_z must be simultaneously present in two orthogonal CT transitions, with the two CT excited states differing only in the occupancy of one orbital. Hence, for 3,4-PCD-PCA, the SOC must be centered on the Fe, resulting in a metal-based SOC mechanism. Since the donors of these two orthogonal transitions are different, the acceptor Fe d orbital has to be common between the two transitions for pseudo-A-term behavior.

From our excited-state calculations, we have found that the experimentally observed LMCTs originate from the PCA and Tyr π_{op} orbitals to the Fe dπ orbitals. Due to the strong covalent interactions between the d_{xz} and the π_{op} PCA orbitals (sym and asym) and between the d_{yz} and the Tyr π_{op} orbital, significant metal characters (d_{xz} and d_{yz}) are observed in the corresponding ligand-based donor MOs (Figure 11). Hence, although the donor CT states are mostly ligand-centered, the metal-based SOC would be operative through the metal contribution in the ligand-based orbitals; i.e., L_zS_z can operate between d_{xz} and d_{yz} on Fe in two different CT states, and this serves as the orbital origin of the excited-state SOC in the 3,4-PCD-PCA complex. To determine which pair of Tyr and PCA to Fe^{3+} CT gives rise to the sign changes observed in the MCD data, we evaluated the sign of the C_0 parameter for each LMCT pair. The procedure involves determining the signs of the transition dipole moment (D_x and D_y) as well as the SOC matrix element L_z and applying these in eq 5. This has been developed in ref 42 and thoroughly presented in ref 78. Application to the DFT-calculated results for the 3,4-PCD-PCA complex gives the following three pairs of LMCT as possibilities for the alternating sign changes observed in the MCD data: (1) PCA π_{op-sym} to d_{xz} $(+C_0)$ and Tyr π_{op} to d_{xz} $(-C_0)$; (2) PCA π_{op-sym} to d_{yz} $(-C_0)$ and Tyr π_{op} to d_{yz} $(+C_0)$; and (3) Tyr π_{op} to d_{xz} $(-C_0)$ and PCA $\pi_{op-asym}$ to d_{xz} $(+C_0)$. These are diagrammed in Figure S3 of the Supporting Information and lead to the specific assignments of bands 1−5

(74) Stephens, P. J. In *Annual Review of Physical Chemistry*; Eyring, H., Ed.; Annual Reviews: Palo Alto, CA, 1974; Vol. 25, pp 201−232.
(75) Osborne, G. A.; Stephens, P. J. *J. Chem. Phys.* **1972**, *56*, 609−618.
(76) Piepho, S. B.; Schatz, P. N. *Group Theory in Spectroscopy with Applications to Magnetic Circular Dichroism*; John Wiley & Sons: New York, 1983.
(77) Gerstman, B. S.; Brill, A. S. *J. Chem. Phys.* **1985**, *82*, 1212−1230.
(78) Yoon, J.; Solomon, E. I. *Coord. Chem. Rev.*, published online April 25, 2006, http://dx.doi.org/10.1016/j.ccr.2006.04.012.

Table 6. Comparison of % Occupancy of Valence PCA Orbitals (Spin-Down) of Ga^{3+}-Catecholate/Semiquinone Complexes and Tyr408-NH_3 Complex with the 3,4-PCD-PCA Complex

model	% occupancy			
	π_{op-sym}	$\pi_{op-asym}$	π_{ip-sym}	$\pi_{ip-asym}$
Ga^{3+}-catecholate	88.23	95.87	83.20	92.62
Ga^{3+}-semiquinone	7.66	94.95	84.58	95.22
Fe^{3+}-PCA	61.47	89.58	86.16	86.63
Fe^{3+}-PCA (Tyr408-NH_3)	47.32	79.04	89.41	85.45

as PCA π_{op-sym} to d_{xz}, PCA π_{op-sym} to d_{yz}, Tyr π_{op} to d_{yz}, Tyr π_{op} to d_{xz}, and PCA $\pi_{op-asym}$ to d_{xz}, respectively.[79] The important part of these assignments is that the lowest energy CT transition is from PCA π_{op} to Fe dπ, which relates to the reactivity of the substrate as developed below.

3.5. Electronic Structure Contributions to Substrate Activation. The main difference among various proposed mechanisms of substrate activation lies in whether the high-spin ferric ES complex has Fe^{2+}-semiquinone or Fe^{3+}-catecholate character. Although the calculated spin densities of the ES complex (Table 5) suggest significant Fe^{2+}-semiquinone character, spin densities can be induced in the PCA unit through spin delocalization from the high-spin Fe^{3+}. Hence, in order to evaluate the effect of spin delocalization through direct bonding interactions, we compared our experimentally calibrated electronic structure of the ES complex with hypothetical Ga^{3+}-substituted catecholate and semiquinone complexes in a ligand environment similar to that in the enzyme active site. Ga^{3+} has an ionic radius similar to that of Fe^{3+} (0.62 vs 0.645 Å, respectively)[30] and is diamagnetic. This allows us to evaluate catecholate and semiquinone ligand−metal bonds in the absence of covalent spin delocalization from the metal. The effect of the Tyr408 ligand on substrate activation is also investigated by comparing the electronic structure of the ES complex with a hypothetical model where Tyr408 is replaced by a weak donor ligand.

A. Catecholate versus Semiquinone Character in the ES Complex. Hypothetical Ga^{3+}-catecholate and Ga^{3+}-semiquinone complexes were formed by replacing the Fe^{3+}, Tyr, and PCA on the ES complex with Ga^{3+}, OH^-, and catecholate while keeping hydrogen-bonding second-sphere Arg residue (modeled as methyl-guanidium ion). The Ga^{3+} complexes were geometry optimized using our experimentally calibrated DFT protocol, and the ligand contributions in the MOs were analyzed (Table 6). For the free ligands, oxidation of catecholate to semiquinone eliminates one electron from the HOMO π_{op-sym} orbital (Figure 9). In the Ga^{3+} complex, the π_{op-sym} β orbital changes from being 88.2% occupied in the Ga^{3+}-catecholate complex to being 7.7% occupied in the Ga^{3+}-semiquinone complex. Occupation differences in the other three donor orbitals are insignificant. Hence, upon oxidation of catecholate to semiquinone in the Ga^{3+} complexes, 0.81 e^- is lost from the π_{op-sym} orbital, with the remaining 0.19 e^- distributed over other ligand orbitals due to binding. Applying this as a reference to the ferric complex, we were able to quantify the amount of catecholate and semiquinone character present in the ES complex (Table 6). Significant changes in the % occupancy relative to the Ga^{3+}-catecholate complex are observed in all four of the valence donor orbitals of PCA in the ES complex, but the degree of difference varies among the orbitals. The π_{op-sym} orbital is 61.5% occupied; thus, only 0.27 e^- is lost from the π_{op-sym} orbital relative to the Ga^{3+}-catecholate complex. Including the other three valence orbitals, the net electron loss of PCA upon binding to the Fe^{3+} center is 0.36 e^-. This net electron loss is much smaller than that observed on the oxidation of the catecholate ligand in the Ga^{3+} complex to semiquinone. In additional, in contrast to the Ga^{3+} complexes, where the electron loss is localized on one orbital (π_{op-sym}), the net electron loss in the ES complex is distributed unequally among the four valence orbitals. Thus, the ES complex is best described as an Fe^{3+}-catecholate complex with very strong covalent interactions, and the covalency is distributed among the four valence donor orbitals.

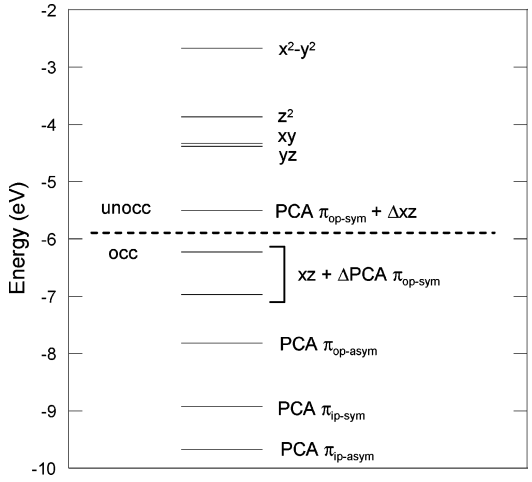

Figure 12. Energy level diagram (spin-down) of the Tyr408-NH_3 complex. Geometry optimized with BP86 + 10% HF exchange with basis set 6-31G*/3-21G* in Gaussian. Note that Δ represents substantial (~25%) mixing of PCA π_{op-sym} and d_{xz} orbitals into the HOMO and LUMO, respectively.

B. The Role of Tyr408 in Substrate Activation. Recent studies on Tyr408 mutants showed that Tyr408 is critical for the dissociation of Tyr447, which allows for the bidentate binding of PCA and facilitates the initial O_2 attack.[22] To evaluate the electronic effect of Tyr408 on substrate activation in the ES complex, a hypothetical model was formed by replacing the 4-Me-phenolate which models Tyr408 by a weaker donor ligand (NH_3). This hypothetical complex (Tyr408-NH_3) was geometry optimized, and the ligand contributions in the MOs were analyzed (Table 6 and Figure 12). The π_{op-sym} orbital changes from being 61.5% occupied in the ES complex to being 47.3% occupied in the Tyr408-NH_3 complex, and the $\pi_{op-asym}$ orbital changes from being 89.6% occupied in the ES complex to being 79.0% occupied in the Tyr408-NH_3 complex. Insignificant changes were noted in the two PCA π_{ip} orbitals. Applying the reference developed in the previous section, the net electron loss of PCA upon binding to the Fe^{3+} in this Tyr408-NH_3 complex is 0.59 e^-. This is much greater than the 0.36 e^- in the ES complex, implying that the Tyr408-NH_3 computational model has more Fe^{2+}-semiquinone character than the ES complex. This is consistent with the difference in ligand donor strength between NH_3 and phenolate. The phenolate imposes a stronger trans influence on the PCA ligand and hence reduces the amount of charge donation from the substrate to the Fe^{3+} center. Thus, Tyr408 appears to play a role in stabilizing the Fe^{3+} center in the active site. When Tyr is not present, the β

(79) Note the change in energy ordering of the acceptor orbitals in the Tyr π_{op}-to-Fe^{3+} LMCT. This is due to excited-state electronic relaxation and is observed in the TD-DFT calculations.

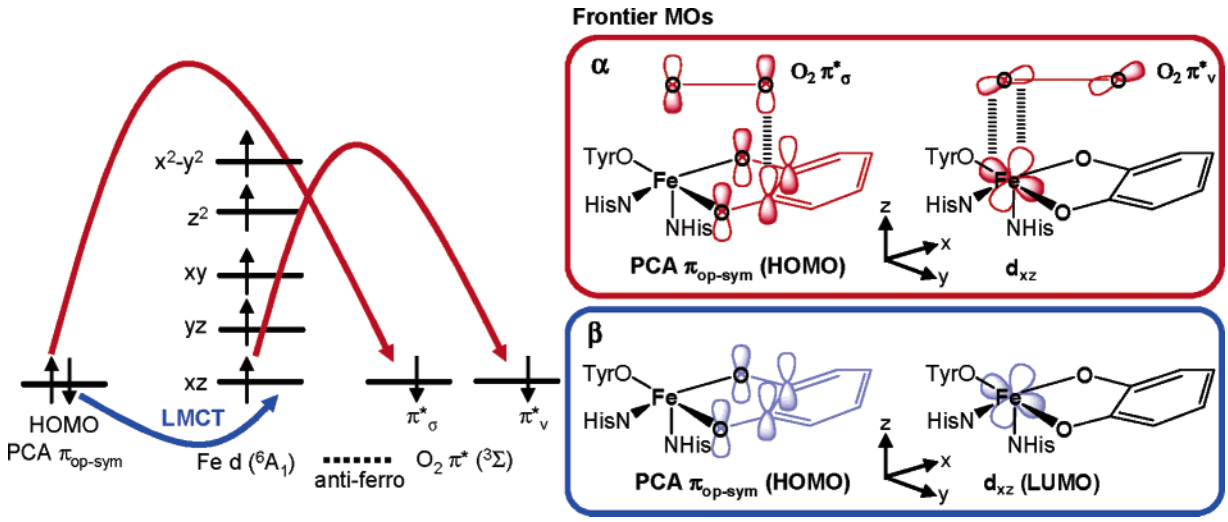

Figure 13. Schematics and the frontier molecular orbitals which participate in the three-electron-transfer process upon O_2 binding.

HOMO shifts from the PCA π_{op-sym} orbital to the Fe d_{xz} orbital (Figure 12). The effect of a more reduced Fe center on the two-electron transfer from the singlet PCA to the triplet O_2 will be discussed below.

C. Frontier Molecular Orbitals and Electrophilic Attack of O_2 on the Substrate. A peroxy adduct bridging between the Fe center and one of the hydroxyl carbons on the catecholic substrate has been proposed to form in the initial step of the O_2 reaction for intradiol dioxygenases.[20] A two-electron transfer between the ES complex and O_2 must accompany the formation of this peroxy intermediate. As shown in the energy level diagram, the doubly occupied PCA π_{op-sym} orbital is the HOMO in the ES complex, with the α orbital being slightly less stable than its β counterpart (Figure 7). This suggests that the high-lying π_{op-sym} orbital can readily donate electrons into the O_2 π^* orbitals (π^*_σ and π^*_v, where σ is oriented along the $O-C^{PCA}$ bond and v is oriented perpendicular (vertical) to this $O-C^{PCA}$ bond), resulting in an electrophilic attack of O_2 on the substrate. However, since the ground state of O_2 is $^3\Sigma_g^-$, the interaction between O_2 and the PCA is spin-forbidden. Only one electron from the doubly occupied π_{op-sym} orbital can be donated directly to the O_2 π^*_σ orbital to form the $C^{PCA}-O$ σ bond. The second electron required to reduce O_2 to O_2^{2-} has to be donated from either another valence PCA orbital or an occupied d orbital of the Fe^{3+} center, which can interact with the π^*_v orbital of O_2 (perpendicular to the $O-C^{PCA}$ direction). NPA charges on the two hydroxyl carbons are both positive, with $C3^{PCA}$ being slightly less positive than $C4^{PCA}$ (C3, 0.21; C4, 0.26). This suggests that C3 (along the *y*-axis of the **D**-tensor described in section 3.2) is the more favorable site for electrophilic attack.

To determine which frontier molecular orbitals participate in the initial interaction with O_2, we inspected the four valence PCA orbitals as well as the five iron d orbitals in both the α and β manifolds. The strong covalent interaction between the PCA π_{op-sym} and d_{xz} orbitals in the β manifold, reflected by the low-energy LMCT transition observed in our spectroscopic data (band 1, Figure 2), shows significant transfer of the β electron from the occupied PCA π_{op-sym} orbital to the unoccupied d_{xz} orbital. This leaves the higher energy α electron of the PCA π_{op-sym} orbital more vulnerable to electrophilic attack by the O_2 π^*_σ orbital and puts the triplet O_2 in an anti-ferromagnetic state relative to the high-spin Fe^{3+} center. This anti-ferromagnetic coupling between O_2 and the high-spin Fe^{3+} center would facilitate the transfer of an α electron from the iron to complete the two-electron redox process between the ES complex and O_2. The iron d orbital which participates in the second electron transfer has to have good overlap with the singly occupied O_2 π^*_v. Among the five d orbitals, the d_{xz} orbital is capable of forming a good π interaction with the O_2 π^*_v orbital. Hence, the transfer of these three electrons (one β and two α) as O_2 binds to the ES complex (Figure 13) demonstrates that the iron center acts as a buffer to transfer an electron pair from the PCA π_{op-sym} orbital to the triplet O_2 in this formally spin-forbidden reaction, which would leave an intermediate spin state ($S = {}^3/_2$) on the Fe^{3+} center.

In the Tyr408-NH_3 complex, the absence of the phenolate ligand leads to strong donation of the PCA π_{op-sym} into the Fe d_{xz} orbital and results in an iron center with more Fe^{2+} character. The PCA π_{op-sym} orbital becomes singly occupied, with the electron residing in the α orbital, and the d_{xz} orbital becomes the HOMO in the β manifold (Figure 12). With the β d_{xz} orbital being the HOMO and of much higher energy than its α counterpart, electrophilic attack of the O_2 π^*_v orbital on the β d_{xz} would become facile. This would stabilize the triplet O_2 in a ferromagnetic configuration relative to the high-spin Fe^{3+} center and restrict the transfer of the α electron from the PCA π_{op-sym} to the O_2 π^*_σ for completing the two-electron redox process between PCA and O_2 (Figure 14). This is different from the anti-ferromagntic arrangement between O_2 and the high-spin Fe^{3+} center in the ES complex. Hence, the presence of Tyr408 helps to stabilize the Fe^{3+} center, which is essential in directing the electrophilic O_2 to attack the PCA π_{op-sym} HOMO and align the triplet O_2 to the correct spin to allow for the second electron transfer between PCA and O_2.

4. Discussion

A combination of spectroscopic techniques (Abs, CD, MCD, and VTVH MCD) and DFT calculations were used here to develop an understanding of the substrate interaction with the Fe^{3+} site in the intradiol dioxygenases. A broad Abs spectrum is present for 3,4-PCD-PCA in the 6000−31000 cm^{-1} region, which we were able to resolve into at least five individual transitions with VTVH MCD. The orbital origins of these LMCT transitions were then investigated by comparing the experimental

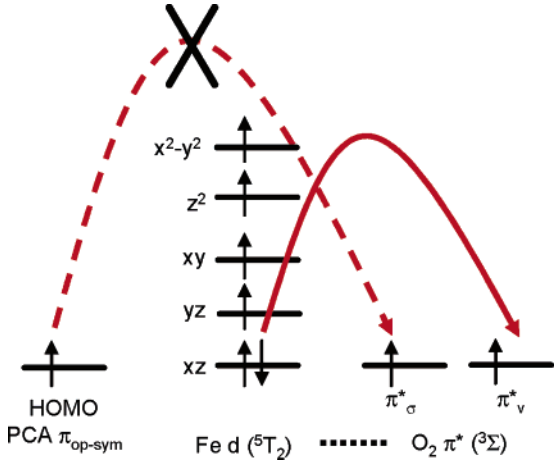

Figure 14. Schematics of electron transfer with Fe^{2+}-semiquinone as the initial electronic description for the ES complex.

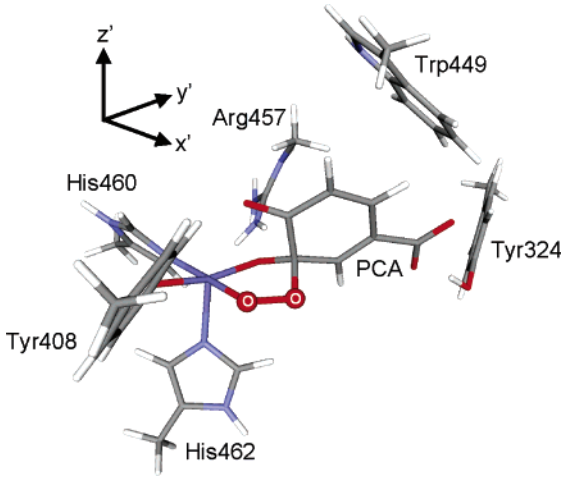

Figure 15. Geometry-optimized peroxy adduct ESO_2 with $S_{tot} = {}^3/_2$ and its coordinate system.

transition energies and the signs of the MCD signal with wave functions and predicted transition dipole moments of the 3,4-PCD-PCA complex obtained from DFT calculations. This showed that all five LMCT transitions originate from charge transfer from the PCA and Tyr π_{op} orbitals to the ferric dπ (*xz* and *yz*) orbitals. These strong π covalent donor bonds between tyrosine/catechol π_{op} orbitals and the iron d_{xz} and d_{yz} orbitals dominate the bonding interaction in the ES complex and are the origins of the pseudo-A-terms observed in our MCD data.

By modeling the three second-sphere residues (Arg457, Tyr324, and Trp449) which either impose steric or hydrogen-bonding interactions to the PCA substrate in our DFT calculations, we were able to reproduce the folded asymmetric binding of PCA to the Fe^{3+} center in the active site of 3,4-PCD. Failure to reproduce the unique geometry of the substrate in the calculations which included only the first coordination sphere residues suggests that the trans influence from Tyr408 alone is not enough to induce the asymmetric binding of the catecholate, which has previously been suggested to assist ketonization of the substrate for O_2 attack.[20] By replacing Tyr408 with NH_3, we found that Tyr408 is essential in stabilizing the Fe^{3+} center in the ES complex for the reaction of O_2 with the HOMO PCA π_{op-sym} orbital to allow for facile electron transfer.

Comparing the electronic structure of 3,4-PCD-PCA with those of the hypothetical Ga^{3+}-catecholate and Ga^{3+}-semiquinone complexes, we found that 3,4-PCD-PCA is best described as a highly covalent Fe^{3+}-catecholate complex where the covalency is distributed unevenly among the four PCA valence orbitals, with the strongest interaction present between the π_{op-sym} and Fe d_{xz} orbitals. This strong π interaction, as reflected in the lowest energy PCA-to-Fe^{3+} LMCT transition (band 1, Figure 2), serves as the origin of substrate activation in the O_2 reaction of intradiol dioxygenases. The transfer of the β electron from the occupied PCA π_{op-sym} orbital to the unoccupied d_{xz} orbital leaves the higher energy α electron of the PCA π_{op-sym} orbital more vulnerable to electrophilic attack by the O_2 π^*_σ orbital. This arranges the triplet O_2 in an antiferromagnetic configuration relative to the high-spin Fe^{3+} center and allows for the interaction between the O_2 π^*_v and Fe d_{xz} orbitals to complete the two-electron redox process between PCA and O_2 in forming the peroxy-bridged adduct. The transfer of these three electrons (one β and two α) to bind O_2 as peroxide to the ES complex (Figure 13) demonstrates that the iron center can act as a buffer in the transfer of an electron pair from singlet PCA to triplet O_2. We have found that the ligand field of Fe is key in overcoming the spin-forbidden nature of the O_2 reaction by stabilizing the interchange of an electron from the PCA π_{op-sym} orbital to the appropriate spin for the second electron reduction of O_2, leaving an intermediate spin state ($S = {}^3/_2$) on the Fe^{3+} center.

Instead of forming a six-coordinate peroxo-bridged intermediate, preliminary geometry optimization of the $S = {}^3/_2$ ESO_2 complex results in two different five-coordinate species in which PCA binds monodentate to the iron, with the peroxide bridging between the iron center and either the C3 or C4 position of the PCA ligand. Due to the slight charge preference for an electrophilic attack at C3 (section 3.5C), its optimized peroxide-bridged structure is presented in Figure 15. In the optimized-geometry complex, $O4^{PCA}$ has come off from the metal center and results in a square-pyramidal ligand field with the open position trans to His462. This open coordination site is defined as the *z*-axis of the ESO_2 complex. The strong ligand interactions in the *xy*-plane, particularly the short $O^{peroxide}$—Fe bond, raise the energy of the $d_{x^2-y^2}$ orbital in the square-pyramidal ligand field and hence stabilize the intermediate spin on the Fe center and facilitate the multi-electron-transfer mechanism developed above.

A final interesting point is that the location of the open coordination site in the ESO_2 complex coincides with the position of Tyr447 coordination before it dissociated from the Fe^{3+} center upon substrate binding. This suggests that, upon O_2 binding, the active site is readily accessible for the re-coordination of Tyr447 to the Fe^{3+} center. We are currently studying this O_2 reaction coordinate to determine: 1) the factors which influence peroxide bridging at $C3^{PCA}$ versus $C4^{PCA}$, 2) at what step along the reaction coordinate Tyr447 rebinds to the Fe^{3+} center, 3) how this affects the spin state of the Fe^{3+} center, and 4) the factors governing intradiol cleavage.

Acknowledgment. This research was supported by NIH Grants GM40392 (E.I.S.) and GM24689 (J.D.L.). M.Y.M.P. thanks the Natural Sciences and Engineering Research Council of Canada for a postgraduate scholarship.

Supporting Information Available: Cartesian coordinates of the geometry-optimized model of the 3,4-PCD-PCA active site with Gaussian BP86 and LanL2DZ (Table S1); Gaussian resolution and absorption spectra of 3,4-PCD and 3,4-PCD-PCA (Figure S1); overlay of the optimized 3,4-PCD-PCA structures with BP86 (LanL2DZ), BP86 + 10% HF exchange (TZVP), and BP86 + 10% HF exchange (6-31G*/3-21G*) (Figure S2); graphical prediction of the signs of the C_0 parameters of the Tyr and PCA→Fe^{3+} CT transitions (Figure S3); and complete ref 43. This material is available free of charge via the Internet at http://pubs.acs.org.

JA065671X